ACS OMEGA

http://pubs.acs.org/journal/acsodf

Article

Structural, Magnetic, and Mossbauer Parameters' Evaluation of Sonochemically Synthesized Rare Earth Er^{3+} and Y^{3+} Ions-Substituted Manganese−Zinc Nanospinel Ferrites

Munirah A. Almessiere,* Sadik Güner, Hakan Gungunes, Murat Sertkol, Yassine Slimani, Rabail Badar, Sultan Akhtar, Sagar E. Shirsath, and Abdulhadi Baykal

Cite This: *ACS Omega* 2021, 6, 22429−22438

Read Online

ACCESS | Metrics & More | Article Recommendations

ABSTRACT: The effect of Er^{3+} and Y^{3+} ion-co-substituted $Mn_{0.5}Zn_{0.5}Er_xY_xFe_{2-2x}O_4$ (MZErYF) ($x \leq 0.10$) spinel nanoferrites (SNFs) prepared by a sonochemical approach was investigated. Surface and phase analyses were carried out using SEM, TEM, and XRD. Hyperfine parameters were determined by fitting room-temperature (RT) Mossbauer spectra. Magnetic field-dependent magnetization data unveiled the superparamagnetic nature at RT and ferrimagnetic nature at 10 K. RT saturation magnetization (M_S) and calculated magnetic moments (n_B) are 34.84 emu/g and 1.47 μ_B, respectively, and have indirect proportionalities with increasing ion content. M_S and n_B data have a similar trend at 10 K including remanent magnetizations (M_r). The measured coercivities (H_C) are between 250 and 415 Oe. The calculated squareness ratios are in the range of 0.152−0.321 for NPs and assign the multidomain nature for NPs at 10 K. The extracted effective magnetocrystalline constants (K_{eff}) have an order of 10^4 erg/g except for $Mn_{0.5}Zn_{0.5}Er_{0.10}Y_{0.10}Fe_{1.80}O_4$ SNFs that has 3.37×10^5 erg/g. This sample exhibits the greatest magnetic hardness with the largest magnitude of H_C = 415 Oe and an internal anisotropy field H_a = 1288 Oe among all magnetically soft NPs.

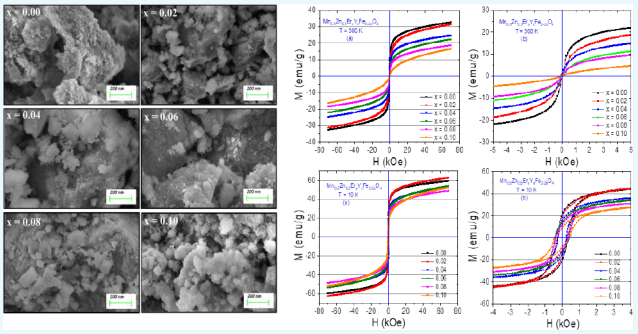

1. INTRODUCTION

Spinel ferrite with formula AB_2O_4 has a cubic structure, where A and B indicate the tetrahedral and octahedral sites, respectively.[1] Spinel ferrite contains 56 atoms in each unit cell distributed among A and B sites.[2,3] The significance of spinel ferrite is because of its wide range of industrial and scientific applications; chemical stability; and the engineering feasibility of tuning its electrical, magnetic, and optical properties. MnZn nanoferrites are a significant category of soft magnetic materials, and their importance has been increasing because of their good electrical, magnetic, and optical properties; high magnetization, resistivity, and initial permeability; permittivity; low power losses; and coercivity. Due to these advantages, MnZn ferrites are fit for use in transformers/transducers, information storage systems, multilayered chip inductors, sensors, biosensor magnetic fluids, refrigerators, mobile chargers, TVs, desktops, printers, microwaves, ovens, LED bulbs, laptops, juicer mixers, washing machines, mobile phones, drug delivery, MRI, etc.[4−9]

The doping of Mn−Zn ferrites, which have a mixed spinel structure, by transition metal ions remarkably influences the structure and optical, electrical, and magnetic attributes. These features depend on the method of preparation, chemical composition, distribution of cations between two interstitial sites, the additives or substitutions, and grain size.[10−13] The inhomogeneous cation distribution and rare earth (RE) substitution can produce a lattice enlargement due to the differences in the Fe^{3+}−Fe^{2+} superexchange interactions and maintain the symmetry of the spinel crystal lattice.[14] The larger ionic radii and the stable 3+ charge of RE ions can give rise to distortions in the crystal structure and the magnetic coercivity and enhance the structural, magnetic, and electrical features.[15] When spinel ferrites are doped by RE ions, 4f−3d coupling determines the magnetocrystalline anisotropy of the products. The Mn−Zn ferrites doped by RE ions show high resistivity and enhanced magnetic features. However, special attention must be paid to the procedure of synthesis. It is essential that the spinel crystal structure suffers major deformation because of the solubility limit of the large amount of RE substitution; accordingly, specific ratios of dopant were chosen. The effect

Received: June 29, 2021
Accepted: August 12, 2021
Published: August 19, 2021

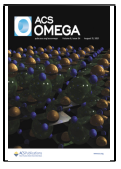

of neodymium (Nd^{+3}) on the magnetic and electrical features of MnZn ferrite was studied by Naik et al.[16,17] Angadi et al.[18] studied the magnetic properties of Sm- and Gd-doped MnZn nanoparticles. Jadhav et al.[19] studied Gd-doped MnZn NPs as magnetic carriers for magnetic fluid hyperthermia (MFH). A comparison study of ultrasonic and sol−gel synthesis of Dy-Y-co-substituted MnZn ferrites was performed by Almessiere et al.[20] There are many synthesis methods for the synthesis of MnZn ferrites, such as solid-state, sol−gel, hydrothermal, co-precipitation, microwave, ultrasonic synthesis, etc. During the ultrasonic synthesis of MnZn ferrites, the following advantages are obtained: the decrease of the reaction time, enhanced reaction rate, the crystal size distribution control, avoidance of agglomeration of nanoparticles, and so on.[21]

Accordingly, no reports have been found on erbium- and yttrium-co-doped Mn−Zn ferrites to date. Therefore, in this study, the structural, magnetic, and Mossbauer parameters of nanocrystalline RE Er^{3+}- and Y^{3+}-co-substituted manganese zinc nanospinel ferrites were deeply investigated.

2. RESULTS AND DISCUSSION

2.1. Structure. XRD patterns of MZErYF ($x \leq 0.10$) spinel nanoferrites (SNFs) are represented in Figure 1. All patterns

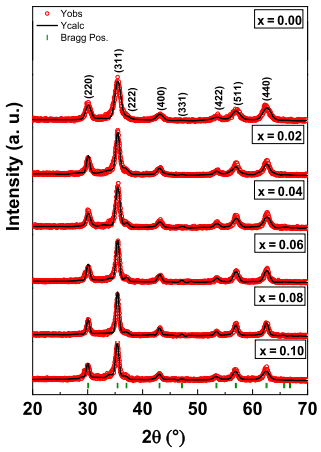

Figure 1. XRD powder patterns of MZErYF ($x \leq 0.10$) SNFs.

indicated the formation a pure phase of cubic Mn−Zn spinel ferrites according to ICDD card no. 00-010-0319, devoid of any impurity. Broad peaks were noticed in all XRD patterns. Due to the nature of the sonochemical synthesis approach, all XRD patterns presented broad XRD peaks, which confirmed the small crystallite sizes of all products. The cell constants are determined via refinement with Match3! and Full-proof, as listed in Table 1. Moreover, the XRD patterns showed the effective incorporation of Er^{3+} (∼0.103 nm) and Y^{3+} (∼0.104 nm) ions into the spinal lattice. The average crystallite sizes were computed by means of the Debye−Scherrer relation and were found to be in the range of 7−13 nm. The cell constant "a_o" increases with increasing "x" value. This increase in the lattice constant of "a_o" is due to the nonconformity in the ionic radii of the Er^{3+} (∼0.103 nm) and Y^{3+} (∼0.104 nm) ions and the host Fe^{3+} (∼0.064 nm) ions in the octahedral sites, which caused the expansion of the unit cell due to the induced strain in the lattice.[22−24]

The cation distribution in spinel ferrite can be obtained from the analysis of the X-ray diffraction pattern. In the present work, the Bertaut method is used to determine the cation distribution.[25,26] This method selects a few pairs of reflections according to the expression

$$\frac{I_{hkl}^{obs.}}{I_{h'k'l'}^{obs.}} = \frac{I_{hkl}^{calc.}}{I_{h'k'l'}^{calc.}} \quad (1)$$

where $I_{hkl}^{obs.}$ and $I_{hkl}^{calc.}$ are the observed and calculated intensities for reflection (hkl), respectively. The best information on cation distribution is achieved when comparing experimental and calculated intensity ratios for reflections whose intensities (i) are nearly independent of the oxygen parameter, (ii) vary with the cation distribution in opposite ways, and (iii) do not differ significantly.

In the present work, the (220), (400), and (440) planes were used to calculate the intensity ratio. These planes are assumed to be sensitive to the cation distribution. The temperature and absorption factors are not taken into account in our calculations as they do not affect the intensity calculation. If an agreement factor (R) is defined as in eq 2, the best-simulated structure that matches the actual structure of the sample leads to a minimum value of R and the corresponding cation distribution is obtained for each hkl and $h'k'l'$ reflection pair considered

$$R = \left| \left(\frac{I_{hkl}^{obs.}}{I_{h'k'l'}^{obs.}} \right) - \left(\frac{I_{hkl}^{calc.}}{I_{h'k'l'}^{calc.}} \right) \right| \quad (2)$$

For the calculation of the relative integrated intensity (I_{hkl}) of a given diffraction line from powder specimens as observed using a diffractometer with a flat-plate sample holder, the following formula is valid

$$I_{hkl} = |F|_{hkl}^2 P L_P \quad (3)$$

where F is the structure factor, P is the multiplicity factor, and L_P is the Lorentz-polarization factor, and

$$L_P = \frac{1 + \cos^2 2\theta}{\sin^2 \theta \cos 2\theta} \quad (4)$$

The obtained cation distributions of the MZErYF ($x \leq 0.10$) SNFs are tabulated in Table 2. Mn preferred the Td

Table 1. Refined Cell Parameters for MZErYF ($x \leq 0.10$) SNFs

x	a (Å)	V (Å^3)	D_{XRD} (nm) ±0.04	χ^2 (chi^2)	R_{Bragg}
0.00	8.390(1)	590.62	7.23	1.19	1.06
0.02	8.394(6)	591.57	9.67	1.36	0.63
0.04	8.396(7)	592.00	11.14	1.36	2.21
0.06	8.396(8)	592.02	11.33	1.22	4.78
0.08	8.401(1)	592.93	12.59	1.20	1.18
0.10	8.407(6)	594.31	10.87	1.07	1.59

Table 2. Cation Distribution of MZErYF ($x \leq 0.10$) SNFs

x	Td site	Oh site
0.00	$Mn_{0.35}Zn_{0.5}Fe_{0.15}$	$Mn_{0.15}Fe_{1.85}$
0.02	$Mn_{0.3}Zn_{0.5}Fe_{0.2}$	$Mn_{0.2}Er_{0.02}Y_{0.02}Fe_{1.76}$
0.04	$Mn_{0.3}Zn_{0.5}Fe_{0.2}$	$Mn_{0.2}Er_{0.04}Y_{0.04}Fe_{1.72}$
0.06	$Mn_{0.3}Zn_{0.5}Fe_{0.2}$	$Mn_{0.2}Er_{0.06}Y_{0.06}Fe_{1.68}$
0.08	$Mn_{0.3}Zn_{0.5}Fe_{0.2}$	$Mn_{0.2}Er_{0.08}Y_{0.08}Fe_{1.64}$
0.10	$Mn_{0.3}Zn_{0.5}Fe_{0.2}$	$Mn_{0.2}Er_{0.1}Y_{0.1}Fe_{1.60}$

https://doi.org/10.1021/acsomega.1c03416
ACS Omega 2021, 6, 22429−22438

(tetrahedral) site as compared to the Oh (octahedral) site, which is in accordance with the preference to Td sites.[27] As anticipated, Zn ions occupy the Td site only. As expected, Fe^{3+} ions occupy the Oh site, and its occupancy linearly decreased with Er and Y substitution. Er and Y ions occupy the Oh site because of their higher ionic radii.

2.2. Morphology. Figure 2 displays a high-magnification SEM analysis of MZErYF ($x \leq 0.10$) SNFs. The SEM images

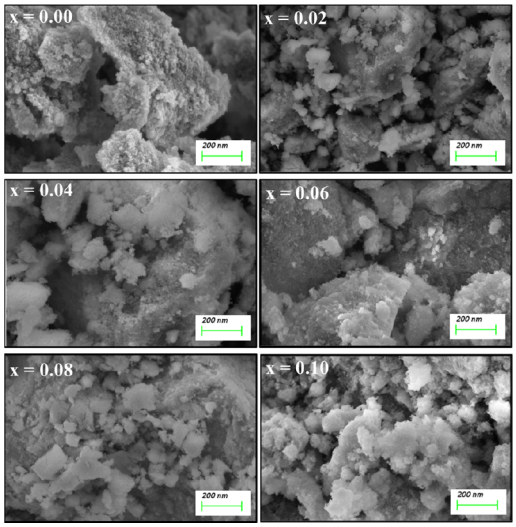

Figure 2. SEM micrographs of MZErYF ($x \leq 0.10$) SNFs.

demonstrated nonuniform clusters of fine spherical particles. It is observed that the aggregation changed with increasing dopant ions as a result of the behavior of nanosized ferrites. The EDX spectra exhibited the weight percentage of the elements in MZErYF ($x \leq 0.10$) SNFs in the absence of undesired elements, as shown in Figure 3. TEM images of MZErYF ($x \leq 0.10$) SNFs are shown in Figure 4. The particles exhibited a cubical structure and appeared aggregated. The histograms show the size distribution between 6 and 24 nm, and the average particle size was estimated to be in the range of 12−20 nm, respectively. The SAED patterns exhibited six well-divided bright rings. These rings are the counterpart of the hkl values of (220), (311), (400), (422), (511), and (440) planes, in agreement with the XRD patterns of Mn−Zn spinel ferrite.

2.3. Magnetic Properties. *2.3.1. Mossbauer Study.* The room-temperature (RT) Mossbauer spectra of MZErYF ($x \leq 0.10$) SNFs are depicted in Figure 5, which were fitted to obtain various parameters included in Table 3. The variation of some Mössbauer parameters by x is given in Figure 6. The spectra of all samples were fitted using two doublets. The doublet, which has a smaller isomer shift value, is due to Fe^{3+} ions in the Td site, while the others are due to Fe^{3+} ions in the Oh site.

The doublets in the structure show that the samples exhibit a superparamagnetic (SPM) nature.[28] The isomer shift is caused by the electron interaction among the nucleus and the density of s electron. The isomer shift (IS) of the Oh site is more than that of the Td site as a result of a larger bond length between Fe^{3+} and O in cubic spinel ferrites as compared with tetrahedral sides. According to the reported data, the IS of Fe^{2+} varies between 0.6 and 1.7 mm/s, while that of Fe^{3+} lies in the range of 0.1−0.5 mm/s at RT.[29,30] Our results show that the IS values belong to the Fe^{3+} charge state. The variation of some Mössbauer parameters by x is given in Figure 6, which shows that the IS value of the Td site increases while that of the Oh site decreases with substitution. The increase of the IS value

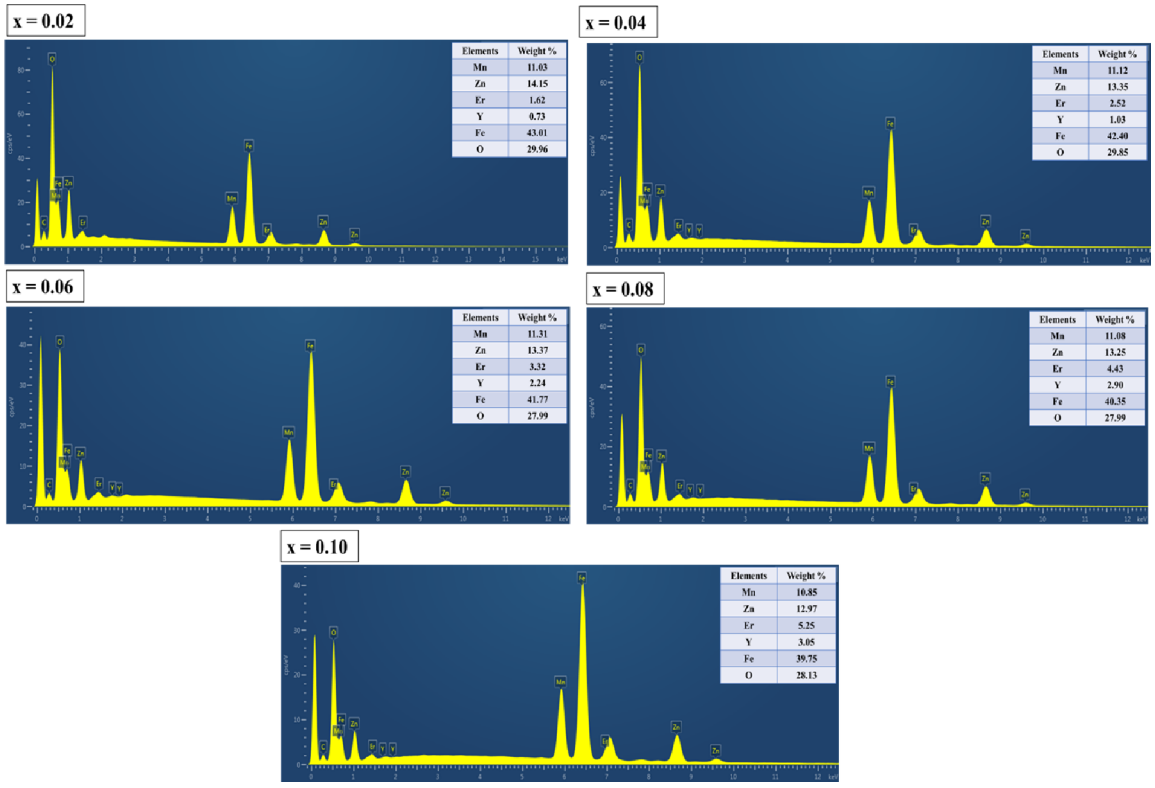

Figure 3. EDX spectra of MZErYF ($x \leq 0.10$) SNFs.

https://doi.org/10.1021/acsomega.1c03416
ACS Omega 2021, 6, 22429−22438

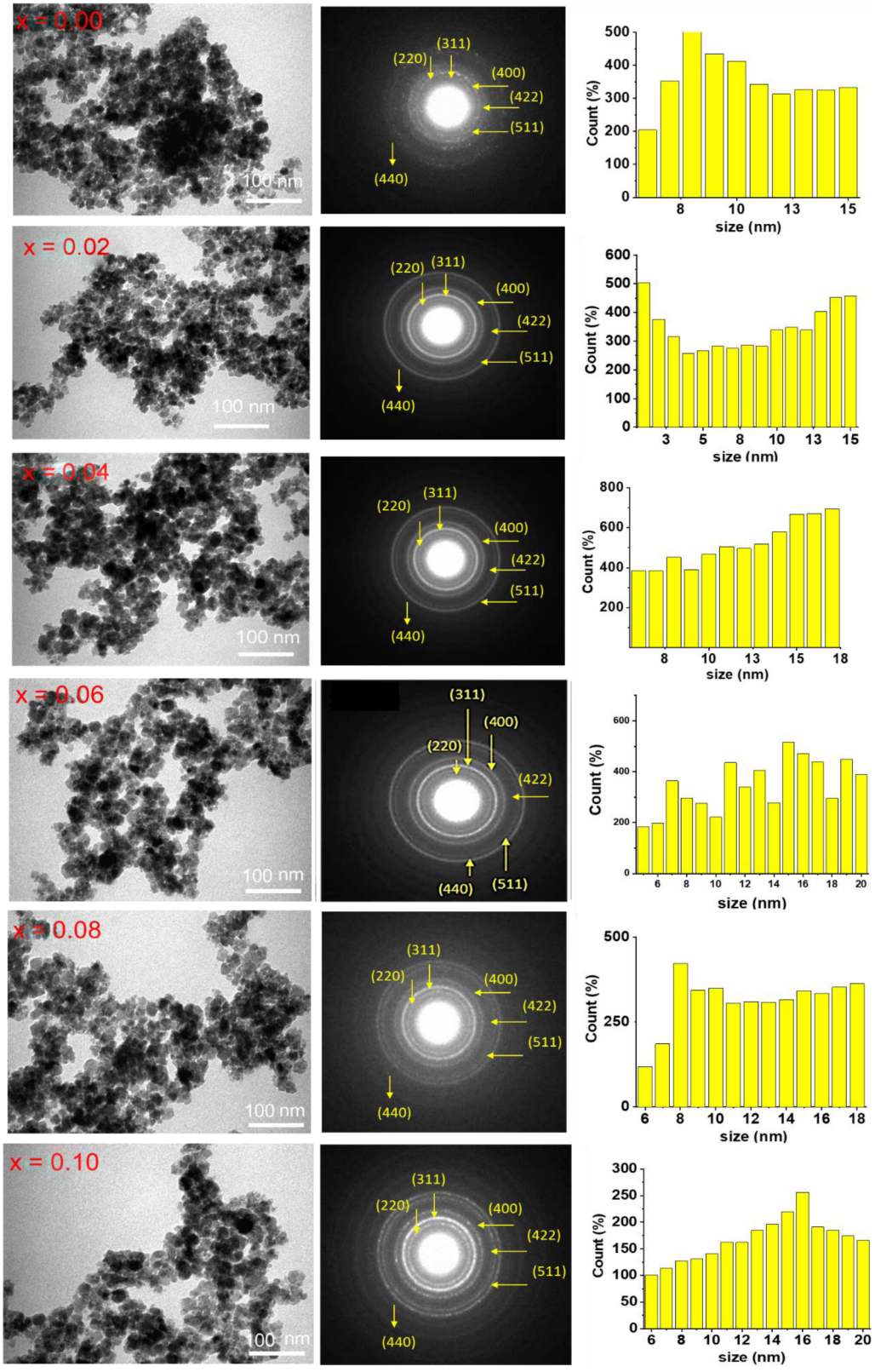

Figure 4. TEM images, SAED patterns, and particle size histograms ($x \leq 0.10$) of SNFs.

illustrates the decrease of the s-electron density at the iron nucleus or vice versa. Therefore, the s-electron density of the iron nucleus at the Td site increases, while that of the Oh site decreases. The isomer shift is also affected by the site volume.[31] The information on the symmetry of the crystal lattice and its local distortions can be gathered from the value of QS. Chemical disorder in the crystal structure is provoked by nonzero quadrupole splitting (QS). The variations of QS reflect distortion of symmetry at Td and Oh sites. According to Table 3, the B/A ratio decreases with increasing Er^{+3} and Y^{+3}

https://doi.org/10.1021/acsomega.1c03416
ACS Omega 2021, 6, 22429−22438

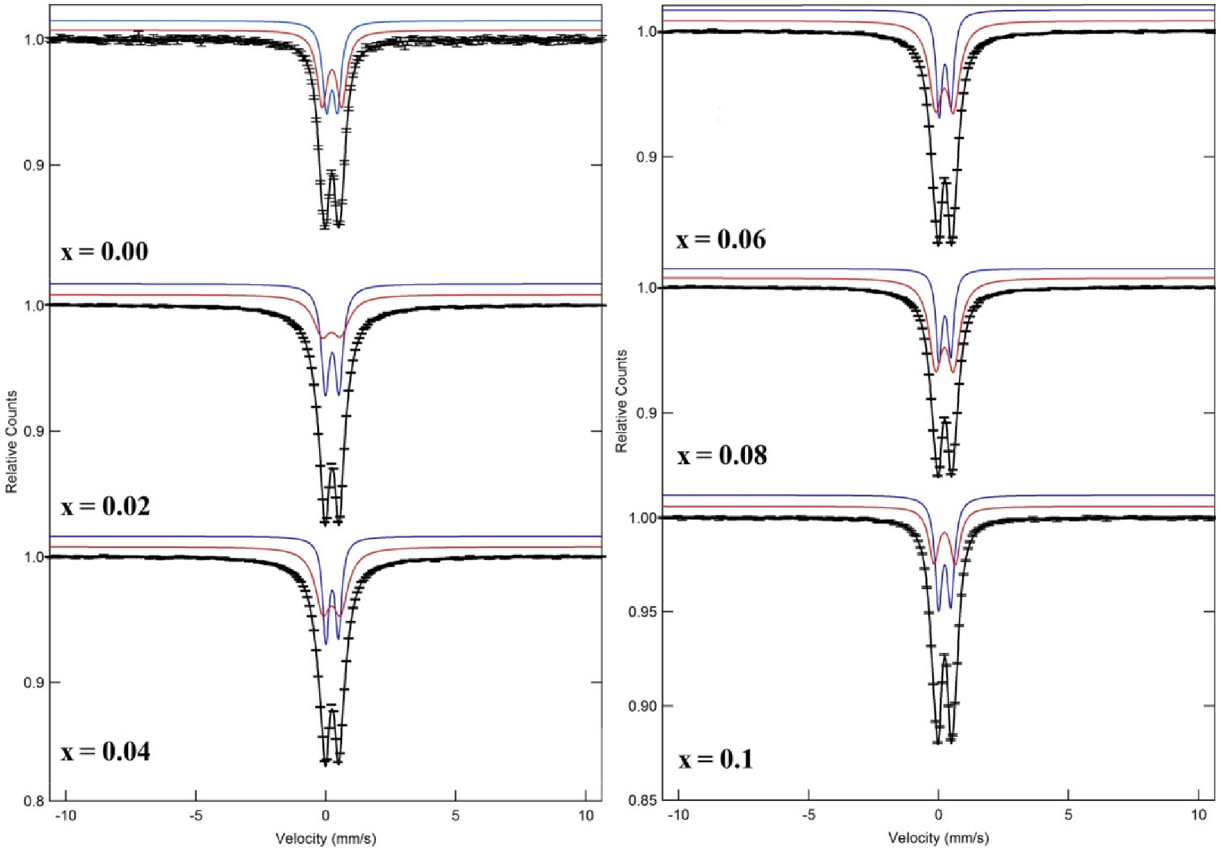

Figure 5. RT Mossbauer spectra of MZErYF ($x \leq 0.10$) SNFs.

Table 3. Mossbauer Parameters of MZErYF ($x \leq 0.10$) SNFs[a]

x	assignment of sites	IS (±0.001) (mm/s)	QS (±0.002) (mm/s)	Γ (±0.01) (mm/s)	R_A (%)
0.00	Db-A:Fe^{3+}	0.340	0.754	0.464	59.529
	Db-B:Fe^{3+}	0.347	0.416	0.361	40.471
0.02	Db-A:Fe^{3+}	0.318	0.726	0.778	60.375
	Db-B:Fe^{3+}	0.349	0.520	0.373	39.625
0.04	Db-A:Fe^{3+}	0.328	0.681	0.705	77.478
	Db-B:Fe^{3+}	0.348	0.487	0.284	22.522
0.06	Db-A:Fe^{3+}	0.329	0.687	0.592	79.290
	Db-B:Fe^{3+}	0.346	0.452	0.268	20.710
0.08	Db-A:Fe^{3+}	0.331	0.688	0.595	81.619
	Db-B:Fe^{3+}	0.342	0.455	0.268	18.381
0.10	Db-A:Fe^{3+}	0.331	0.822	0.467	51.502
	Db-B:Fe^{3+}	0.336	0.464	0.323	48.498

[a]IS, isomer shift; QS, quadrupole splitting; Γ, line width; and R_A, relative area.

content up to x = 0.08 and then increases at x = 0.1. These results are in agreement with the XRD results. These results also show that the Er^{+3} and Y^{+3} ions occupy the Oh site.

2.3.2. Magnetization Investigation. Magnetic investigations were performed for MZErYF ($x \leq 0.10$) SNFs using a vibrating sample magnetometer (VSM) device by recording the field ($M-H$)- and the temperature ($M-T$)-dependent specific magnetizations. $M-H$ data were alsoobtained at 300 and 10 K to collect information about the temperature-dependent dominating magnetic phases. Figure 7 presents the $M-H$ curves recorded at 300 K and under an externally acting DC field of (a) ±70 kOe and (b) enlarged views for the range of ±5 kOe. The typical S-shape spectra, which have a negligible amount of coercivities (H_C) or remnant magnetizations (M_r), are not observed even in enlarged views. This case identifies the presence of a SPM phase for all NPs at 300 K. The single-domain nature is the characteristic feature of nanoparticles that exhibit the SPM phase. All magnetic moments align in a preferential direction determined by the leading type of anisotropy in the structure. That is, a single-domain structured nanoparticle behaves like a single giant magnetic moment having a net spontaneous magnetization M_S. The existence of the SPM phase not only necessitates a critically small dimension of nanoparticles (or grains) but also requires the absence of an adequate magnitude of exchange interactions needed for internal spontaneous magnetization. Further, the absence of interparticle interactions, which stimulate different magnetic phases, is another obligation for a conventional SPM phase. The critical size for $Mn_{0.5}Zn_{0.5}Fe_2O_4$ SNFs to exhibit a SPM nature is reported to be ∼25 nm in the literature.[32,33] Some recorded TEM images reveal the dimension of fabricated SNFs to be smaller than this maximum limit.

Although a 70 kOe applied external field is a rather strong field, spectra do not depict a horizontal alignment assigning the obtained saturation magnetizations (M_S) for NPs. This is why M_S magnitudes were estimated from linear fits to M vs $1/H^2$ plots, as shown in Figure 8. Undoped $Mn_{0.5}Zn_{0.5}Fe_2O_4$ SNFs among ultrasonically fabricated samples have an $M_{S,max}$ value of 34.84 emu/g. The co-doping process with Er^{3+} and Y^{3+} ions decreases the saturation magnetizations, exhibiting almost an indirect proportionality with the increasing ratio of two ions. Hence, it is estimated that $Mn_{0.5}Zn_{0.5}Er_{0.10}Y_{0.10}Fe_{1.80}O_4$ SNFs that have a maximum doping content have a $M_{S,min}$ value of

https://doi.org/10.1021/acsomega.1c03416
ACS Omega 2021, 6, 22429−22438

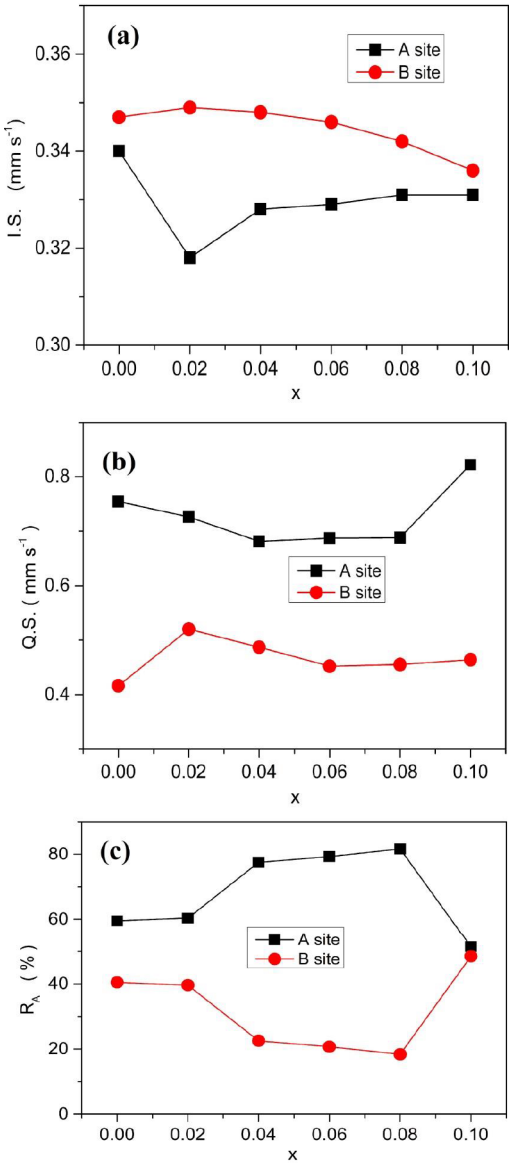

Figure 6. Variations in (a) isomer shift, (b) quadrupole splitting, and (c) relative area with Er−Y substitution in MZErYF ($x \leq 0.10$) SNFs.

19.35 emu/g. The magnetic moment per chemical formula (n_B) was calculated in units of Bohr magneton using the

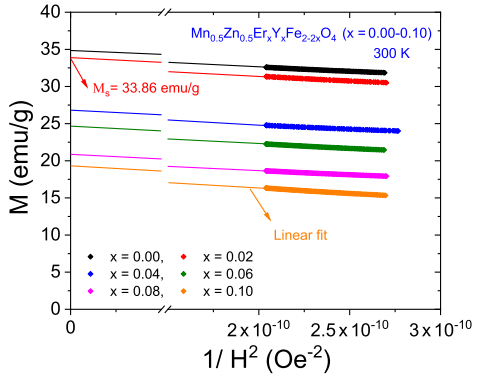

Figure 8. M vs $1/H^2$ plots for MZErYF ($x \leq 0.10$) SNFs at RT.

molecular weight (M_W)- and M_S-dependent equation as given below[22,34,35]

$$n_B = \left(\frac{M_W \times M_S}{5585}\right)(\mu_B) \quad (5)$$

The maximum and minimum magnetic moments of 1.47 and 0.87 μ_B belong to $Mn_{0.5}Zn_{0.5}Fe_2O_4$ NPs and $Mn_{0.5}Zn_{0.5}Er_{0.10}Y_{0.10}Fe_{1.80}O_4$ SNFs, respectively. Due to co-doped ions, the changing content of cations at both tetrahedral and octahedral sites plays a significant role in the resultant magnetic moments. A similar indirect proportionality as observed for the magnetization data is also valid for the experimentally evaluated magnetic moments as a function of the increasing content (x) of co-doped Er^{3+} and Y^{3+} ions. In the literature, the experimentally observed magnetic moment values of Zn^{2+}, Mn^{2+}, Fe^{3+}, Er^{3+}, and Y^{3+} ions are reported to be 0, 4.6, 4.1, 9.5, and 0 μ_B, respectively.[36−38] The increasing content of Er^{3+} ions that are located at the octahedral B site in the reverse direction with a large experimentally observed n_B of 9.5 μ_B might be the main reason for the decreasing magnetic moment and magnetization of the doped samples. All derived magnetic parameters from the $M-H$ spectra that were obtained at 300 K are presented in Table 4.

The $M-H$ hysteresis loops that were recorded at 10 K and their enlarged views for the field range of ±4 kOe are presented in Figure 9a,b, respectively. Figure 9a clearly illustrates that $Mn_{0.5}Zn_{0.5}Er_{0.02}Y_{0.02}Fe_{1.96}O_4$ SNFs have the largest magnetization ability among all samples at 10 K. However, Figure 9b reveals that magnetic NPs do not perpetuate their SPM characteristics at 10 K, and, instead, a

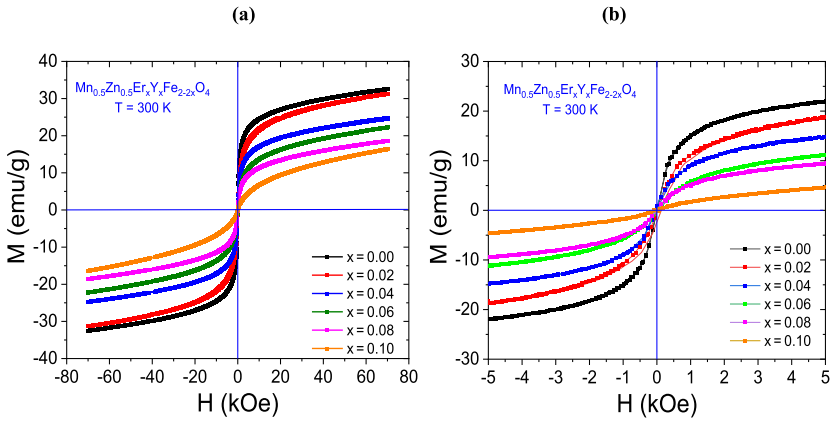

Figure 7. (a) $M-H$ curves of MZErYF ($x \leq 0.10$) SNFs recorded at RT and (b) enlarged view of the magnetization curves.

https://doi.org/10.1021/acsomega.1c03416
ACS Omega 2021, 6, 22429−22438

Table 4. Magnetic Parameters of MZErYF ($x \leq 0.10$) SNFs

		300 K		10 K						
x	M_W (g/mol)	M_S (emu/g)	n_B (μ_B)	M_S (emu/g)	n_B (μ_B)	M_r (emu/g)	H_C (Oe)	SQR (M_r/M_S)	K_{eff} ($\times 10^4$ erg/g)	H_a (Oe)
0.00	235.854	34.84	1.47	62.35	2.63	20.00	361	0.321	3.52	1128
0.02	238.744	33.86	1.45	66.14	2.83	17.20	284	0.260	2.93	888
0.04	241.633	26.88	1.16	55.37	2.40	14.88	250	0.269	2.16	781
0.06	244.523	24.76	1.08	57.95	2.54	13.00	409	0.224	3.72	1284
0.08	247.412	20.84	0.92	51.99	2.30	11.75	378	0.226	3.07	1181
0.10	250.302	19.35	0.87	56.88	2.55	8.63	415	0.152	33.70	1288

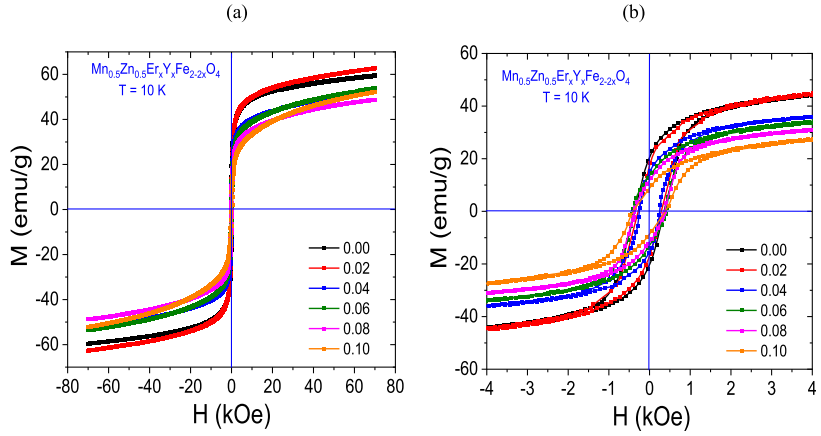

Figure 9. (a) $M-H$ hysteresis loops of MZErYF ($x \leq 0.10$) SNFs recorded at 10 K and (b) enlarged view of these loops.

ferrimagnetic phase as expected from the ferrite NPs is observed. Low-temperature conditions exclude the demagnetizing effect of heat energy on the magnetization process and enable magnetic materials to exhibit their magnetic phases that originate due to moment alignment in the host crystal structure. Undoped $Mn_{0.5}Zn_{0.5}Fe_2O_4$ NPs have the largest remnant magnetization (M_r) of 20 emu/g and a remarkable magnitude of coercivity (H_C) of 361 Oe. Co-doped samples have a decreasing magnitude of M_r values on increasing the ratio of Er^{3+} and Y^{3+} ion contents.

The coercivity field range has a narrow band with $H_{C,min}$ = 250 Oe (belonging to $Mn_{0.5}Zn_{0.5}Er_{0.04}Y_{0.04}Fe_{1.92}O_4$ SNFs) and $H_{C,max}$ = 415 Oe (belonging to $Mn_{0.5}Zn_{0.5}Er_{0.10}Y_{0.10}Fe_{1.80}O_4$ SNFs). However, one can easily claim that the order of the measured coercivities categorizes all pristine or co-doped samples as a member of magnetically soft spinel ferrites. Although ferrimagnetic phases were observed, none of the samples could reach saturated magnetization even under a 70 kOe acting field. Therefore, the order of M_S magnitudes was specified by the intercept of the fitting lines at the magnetization axis as for $1/H^2$ equal to zero, as depicted in Figure 10. Pristine $Mn_{0.5}Zn_{0.5}Fe_2O_4$ NPs have the second largest saturation magnetization of 62.35 emu/g among the 10 K data despite being first among the 300 K saturation data. This determination stimulates the interpretation of the ratio of estimated saturation magnetizations ($M_{S,10\ K}/M_{S,300\ K}$) for all samples by assuming that cationic distributions or lattice defects due to co-doped ions are stable at both 300 and 10 K. Disordered surface spin layers are other mainly observed defects that affect negatively the total magnetic moment and magnetization of $Mn_{0.5}Zn_{0.5}Fe_2O_4$ NPs. The magnitude of the ratio for pristine ferrite is 1.79. On the other hand, the determined ratios are 1.95, 2.06, 2.34, 2.50, and 2.94 corresponding to co-doped ion contents of x = 0.02, 0.04, 0.06, 0.08, and 0.10, respectively. The steadily increasing ratios might be attributed to thicker disordered surface layers with increasing co-doped ion content. One can expect better ordering of these disordered surface spins at 10 K when the demagnetizing effect of heat is excluded at a high ratio. In the literature, strengthening of superexchange interactions is also reported as a reason for increasing magnetization parameters.[22] Another kind of division, that is, M_r/M_S, is described as the dimensionless squareness ratio (SQR), which gives information particularly about the domain feature of the host magnetic material. SQRs start from 0.321 and steadily decrease to 0.152. This range of SQRs is attributed to the multidomain nature of NPs according to the Stoner−Wohlfarth theory.[22,39]

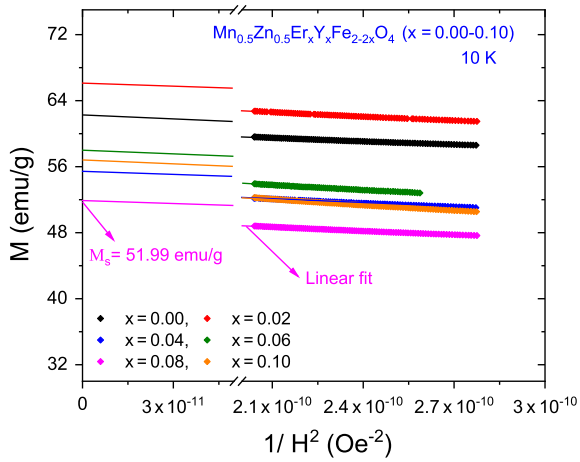

Figure 10. M vs $1/H^2$ plots for MZErYF ($x \leq 0.10$) SNFs.

The internal magnetocrystalline anisotropy field, H_a, is directly responsible for the detection of the coercivity and the degree of magnetic hardness of the material. Once the effective

https://doi.org/10.1021/acsomega.1c03416
ACS Omega 2021, 6, 22429−22438

magnetocrystalline anisotropy constant (K_{eff}) is specified, then the order of the anisotropy field for the fabricated nanoparticle samples can be easily extracted. The following equation relates three magnetic parameters: K_{eff}, measured H_C values, and estimated saturation magnetizations[40]

$$H_c = 0.64\frac{K_{eff}}{M_S} \quad (6)$$

Therefore, we determined K_{eff} values for all samples by substituting the already determined 10 K magnetic data in eq 2. K_{eff} values are in the range of 2.16−3.72 × 10^4 erg/g, except for the $Mn_{0.5}Zn_{0.5}Er_{0.10}Y_{0.10}Fe_{1.80}O_4$ SNFs. Since this sample has the largest coercivity, the determined magnitude of K_{eff} concludes the largest magnitude to be 3.37 × 10^5 erg/g among all NPs too. The internal anisotropy field can be calculated from the following equation:

$$H_a = \frac{2K_{eff}}{M_S}\ (\mathrm{Oe}) \quad (7)$$

Among calculated internal magnetocrystalline anisotropy fields, $H_{a,min}$ = 781 Oe belongs to $Mn_{0.5}Zn_{0.5}Er_{0.04}Y_{0.04}Fe_{1.92}O_4$ SNFs and $H_{a,max}$ = 1288 Oe belongs to $Mn_{0.5}Zn_{0.5}Er_{0.10}Y_{0.10}Fe_{1.80}O_4$ SNFs due to their minimum and maximum coercivity magnitudes as expected. Other samples have internal anisotropies between these two limiting values. Hence, the presence of disordered spins on the surface of nanoparticles and an internal magnetocrystalline anisotropy field (causing coercivity and magnetic hardness) are the main perpetrators in the magnetic host that prevent the observation of saturation magnetization even under high acting fields and at low-temperature conditions. All magnetic parameters derived from 10 K hysteresis loops are reported in Table 4 with 300 K magnetization data.

Figure 11 presents the zero-field cooling (ZFC) and field cooling (FC) magnetization spectra of some previously

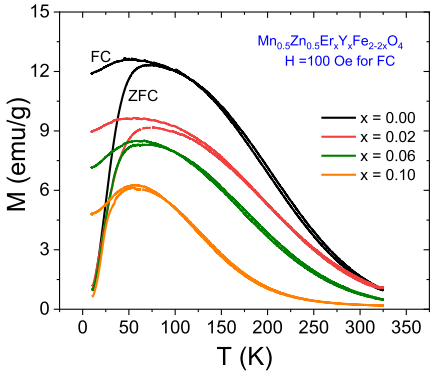

Figure 11. Temperature dependence of ZFC and FC magnetizations for MZErYF (x = 0.00, 0.02, 0.06, and 0.10) SNFs.

determined MZErYF ($x \leq 0.10$) SNFs. For ZFC measurements, samples were first cooled in the zero field until 10 K, and then magnetization data were recorded on increasing the temperature up to 325 K by simultaneously exposing them to a static dc field of 100 Oe. For FC measurements, the same selected samples were cooled in the same field until 10 K and then the FC data were recorded by increasing the temperature up to 325 K without removing the acting static field. The maxima observed in the ZFC spectra provide the magnitude of blocking temperature (T_B) for magnetic NPs. Ferrimagnetic phases are observed below T_B, and above T_B, NPs exhibit a SPM phase consistent with the Cure−Weiss law.[5] In the SPM phase, the coercivity and remnant magnetizations disappear.

The corresponding blocking temperatures for our NPs are 68.6, 66.1, 57.5, and 53.4 K. We observe a slight red shift in T_B values with increasing co-doped ion concentrations. When the temperature decreases below T_B, the antiferromagnetic interactions become stronger in octahedral B sites of spinel ferrite. This case concludes collective spin freezing and an intensive decrease in the magnitude of magnetization. On the other hand, the FC magnetization curve is expected to keep its increasing trend and maximum magnetization should be recorded at a minimum cooling temperature. However, our recorded FC magnetization curves exhibit some decreases below their peak temperature positions. This type of behavior is attributed to the presence of spin-glass-like phases in temperature ranges below T_B.[41] According to XRD and TEM investigations, the particle/crystallite sizes increase with increasing Er^{3+} and Y^{3+} ion ratio. However, a reverse correlation between the increasing particle/crystallite size and the decreasing blocking temperature is observed.

3. CONCLUSIONS

The sonochemical technique was applied for fabrication of MZErYF ($x \leq 0.10$) SNFs. The pure structure of MZErYF SNFs was confirmed via the analyses of XRD patterns. The crystal size was found to be within the range of 7−12 nm. It was found that the cell parameters increased with increased dopant ions due to the enlargement the lattice. The cubic morphology and chemical compositions were revealed using SEM, TEM, EDX, and elemental mappings. According to Mössbauer results, all of the samples exhibit superparamagnetism at RT. The s-electron density of iron nucleus at A and B sites is affected by substitution. The doped ions occupy the octahedral B site. According to $M-H$ investigations, MZErYF ($x \leq 0.10$) SNFs exhibit a single-domain nature at 300 K, and in the ferrimagnetic phase, they exhibit a multidomain nature at 10 K. The co-doping process with Er^{3+} and Y^{3+} ions tunes magnetic data remarkably and mainly results in reduced M_r and M_S values. An indirect proportionality is observed for experimentally detected magnetization parameters as a function of the increasing content (x) of co-doped Er^{3+} and Y^{3+} ions. $Mn_{0.5}Zn_{0.5}Er_{0.02}Y_{0.02}Fe_{1.96}O_4$ SNFs have the largest magnetization among all samples according to 10 K $M-H$ investigations. However, all samples are members of magnetically soft ferrite materials, although $Mn_{0.5}Zn_{0.5}Er_{0.10}Y_{0.10}Fe_{1.80}O_4$ SNFs are the magnetically hardest among them. The fraction between 300 and 10 K saturation magnetizations indictaes the presence of disordered surface spin layers that become thicker with increasing ion concentration. The characteristics of ZFC and FC spectra revealed the presence of collective spin freezing and spin-glass-like behavior below the blocking temperature in M−T investigations. The blocking temperature has indirect proportionalities with increasing co-doped ion content and particle/crystallite size.

4. EXPERIMENTAL SECTION

4.1. Instrumentation. The structure of the products was analyzed using a Benchtop Rigaku Miniflex X-ray diffractometer. Mossbauer spectra were recorded using a spectrometer with a constant acceleration mode of a 10mCi ^{57}Co (Rh

https://doi.org/10.1021/acsomega.1c03416
ACS Omega 2021, 6, 22429−22438

matrix) radiation source. The nanoparticles' morphology was obtained using FEI Titan ST SEM and TEM linked with EDX spectroscopy for elemental analysis. The SAED (selected area electron diffraction) patterns were obtained to study the crystalline structure. The magnetic measurements of samples were performed using a Quantum Design North America PPMS DynaCool-9 system coupled with a VSM.

4.2. Nanomaterial Synthesis. A series of MZErYF ($x \leq 0.10$) SNFs were synthesized using the sonochemical approach. All chemicals were obtained from commercial sources (Merck and US Research Nanomaterials, Inc.). For the typical synthesis, iron(III) nitrate nonahydrate ($Fe(NO_3)_3 \cdot 9H_2O$), manganese(II) nitrate hexahydrate ($Mn(NO_3)_2 \cdot 6H_2O$), zinc nitrate hexahydrate ($Zn(NO_3)_2 \cdot 6H_2O$), erbium nitrate pentahydrate ($Er(NO_3)_3 \cdot 5H_2O$), and yttrium nitrate hexahydrate ($Y(NO_3)_3 \cdot 6H_2O$) were used as the source material for Fe, Mn, Zn, Er, and Y, respectively. Stoichiometric amounts of metal nitrates $Mn(NO_3)_2 \cdot 6H_2O$, $Fe(NO_3)_3 \cdot 9H_2O$, $Zn(NO_3)_2 \cdot 6H_2O$, $Er(NO_3)_3 \cdot 5H_2O$, and $Y(NO_3)_3 \cdot 6H_2O$ were thawed in 50 mL of deionized (DI) H_2O, and the pH was set at 11 using a 2 M NaOH solution; then, they were irradiated using a UZ SONOPULS HD 2070 ultrasonic homogenizer at 20 kHz and 70 W for 40 min (Table 5). At the end of ultrasonication, the reaction temperature was measured to be 90 °C owing to the high number of collisions between the reactants. The obtained product was washed several times with DI water. The magnetic solid product was separated from the liquid using a simple external magnet and was then dried at 60 °C for 12 h.[21,22] No calcination process was applied to the products. This was the main advantage of this synthesis procedure.

Table 5. Number of Moles of Each Element Used during the Synthesis of Each Product

x	Mn	Zn	Er	Y	Fe
0.00	0.5	0.5			2
0.02	0.5	0.5	0.02	0.02	1.96
0.04	0.5	0.5	0.04	0.04	1.92
0.06	0.5	0.5	0.06	0.06	1.88
0.08	0.5	0.5	0.08	0.08	1.84
0.1	0.5	0.5	0.1	0.1	1.80

AUTHOR INFORMATION

Corresponding Author

Munirah A. Almessiere − *Department of Physics, College of Science, Imam Abdulrahman Bin Faisal University, Dammam 31441, Saudi Arabia; Department of Biophysics, Institute for Research and Medical Consultation (IRMC), Imam Abdulrahman Bin Faisal University, Dammam 31441, Saudi Arabia;* orcid.org/0000-0003-1651-3591; Email: malmessiere@iau.edu.sa

Authors

Sadik Güner − *Institute of Inorganic Chemistry, RWTH Aachen University, 52074 Aachen, Germany*

Hakan Gungunes − *Department of Physics, Hitit University, 19030 Çorum, Turkey*

Murat Sertkol − *Department of Basic Science, Deanship of Preparatory Year and Supporting Studies, Imam Abdulrahman Bin Faisal University, Dammam 34212, Saudi Arabia*

Yassine Slimani − *Department of Biophysics, Institute for Research and Medical Consultation (IRMC), Imam Abdulrahman Bin Faisal University, Dammam 31441, Saudi Arabia;* orcid.org/0000-0002-2579-1617

Rabail Badar − *Université Toulouse III - Paul Sabatier, 31062 Toulouse, CEDEX 9, France*

Sultan Akhtar − *Department of Biophysics, Institute for Research and Medical Consultation (IRMC), Imam Abdulrahman Bin Faisal University, Dammam 31441, Saudi Arabia*

Sagar E. Shirsath − *School of Materials Science and Engineering, University of New South Wales, Sydney, New South Wales 2052, Australia;* orcid.org/0000-0002-2420-1144

Abdulhadi Baykal − *Department of Nanomedicine Research, Institute for Research and Medical Consultation (IRMC), Imam Abdulrahman Bin Faisal University, Dammam 31441, Saudi Arabia*

Complete contact information is available at: https://pubs.acs.org/10.1021/acsomega.1c03416

Notes

The authors declare no competing financial interest.

ACKNOWLEDGMENTS

The authors are thankful to the Institute for Research and Medical Consultations (IMRC) of Imam Abdulrahman BinFaisal University (IAU, Saudi Arabia) for providing lab facilities. This work was financially supported by the Deanship for Scientific Research (project application no. 2020-164-IRMC) of Imam Abdulrahman Bin Faisal University (IAU, Saudi Arabia).

REFERENCES

(1) Karimunnesa, S.; Ullah, A. K. M. A.; Hasan, M. R.; Shanta, F. S.; Islam, R.; Khan, M. N. I. Effect of holmium substitution on the structural, magnetic and transport properties of $CoFe_{2-x}Ho_xO_4$ ferrites. *J. Magn. Magn. Mater.* **2018**, *457*, 57−63.

(2) Snelling, E. C. *Soft Ferrites: Properties and Applications*, 1st ed.; Iliffe: London, 1969; pp 1−385.

(3) Smit, J. *Magnetic Properties of Materials*; McGraw-Hill: New York, 1971; pp 1−448.

(4) Thakur, P.; Chahar, D.; Taneja, S.; Bhalla, N.; Thakur, A. A review on MnZn ferrites: Synthesis, characterization and applications. *Ceram. Int.* **2020**, *46*, 15740−15763.

(5) Almessiere, M. A.; Slimani, Y.; Rehman, S.; Khan, F. A.; Güngüneş, Ç. D.; Güner, S.; Shirsath, S. E.; Baykal, A. Magnetic properties, anticancer and antibacterial effectiveness of sonochemically produced Ce^{3+}/Dy^{3+} co-activated Mn-Zn nanospinel ferrites. *Arabian J. Chem.* **2020**, *13*, 7403−7417.

(6) Angadi, V. J.; Choudhury, L.; Sadhana, K.; Lin Liu, H.; Sandhya, R.; Matteppanavar, S.; Rudraswamy, B.; Pattar, V.; Anavekar, R. V.; Praveena, K. Structural, electrical and magnetic properties of Sc^{3+} doped Mn-Zn ferrite nanoparticles. *J. Magn. Magn. Mater.* **2017**, *424*, 1−11.

(7) Praveena, K.; Sadhana, K.; Bharadwaj, S.; Murthy, S. R. Development of nanocrystalline Mn−Zn ferrites for high frequency transformer applications. *J. Magn. Magn. Mater.* **2009**, *321*, 2433−2437.

(8) Praveena, K.; Sadhana, K.; Murthy, S. R. Elastic behaviour of microwave hydrothermally synthesized nanocrystalline $Mn_{1-x}Zn_x$ ferrites. *Mater. Res. Bull.* **2012**, *47*, 1096−1103.

(9) Praveena, K.; Murthty, S. R. Magneto acoustical emission in nanocrystalline Mn−Zn ferrites. *Mater. Res. Bull.* **2013**, *48*, 4826−4833.

(10) Praveena, K.; Sadhana, K.; Bharadwaj, S.; Murthy, S. R. Fabrication of dc−dc converter using nanocrystalline Mn−Zn ferrites. *Mater. Res. Innovations* **2010**, *14*, 102−106.
(11) Praveena, K.; Sadhana, K.; Bharadwaj, S.; Murthy, S. R. Development of nanocrystalline Mn−Zn ferrites for forward type DC−DC converter for switching mode power supplies. *Mater. Res. Innovations* **2010**, *14*, 56−61.
(12) Praveena, K.; Sadhana, K.; Virk, H. S. Structural and magnetic properties of Mn-Zn ferrites synthesized by microwave-hydrothermal process. *Solid State Phenom.* **2015**, *232*, 45−64.
(13) Islam, R.; Hakim, M. A.; Rahman, M. O.; Narayan Das, H.; Mamun, M. A. Study of the structural, magnetic and electrical properties of Gd-substituted Mn−Zn mixed ferrites. *J. Alloys Compd.* **2013**, *559*, 174−180.
(14) Abdellatif, M. H.; Azab, A. A.; Salerno, M. Effect of rare earth doping on the vibrational spectra of spinel Mn-Cr ferrite. *Mater. Res. Bull.* **2018**, *97*, 260−264.
(15) Zhao, L.; Yang, H.; Yu, L.; Cui, Y.; Zhao, X.; Feng, S. Magnetic properties of resubstituted Ni−Mn ferrite nanocrystallites. *J. Mater. Sci.* **2007**, *42*, 686−691.
(16) Naik, P. P.; Hasolkar, S. S.; Kothawale, M. M.; Keluskar, S. H. P. Altering saturation magnetization of manganese zinc ferrite nanoparticles by doping with rare earth Nd^{+3} ions. *Phys. B* **2020**, *584*, No. 412111.
(17) Naik, P. P.; Tangsali, R. B. Enduring effect of rare earth (Nd^{3+}) doping and γ-radiation on electrical properties of nanoparticle manganese zinc ferrite. *J. Alloys Compd.* **2017**, *723*, 266−275.
(18) Angadi, V. J.; Manjunatha, K.; Praveena, K.; Pattar, V. K.; Fernandes, B. J.; Manjunatha, S. O.; Husain, J.; Angadi, S. V.; Horakeri, L. D.; Ramesh, K. P. Magnetic properties of larger ionic radii samarium and gadalonium doped manganese zinc ferrite nanoparticles prepared by solution combustion method. *J. Magn. Magn. Mater.* **2021**, *529*, No. 167889.
(19) Jadhav, S. V.; Shewale, P. S.; Shin, B. C.; Patil, M. P.; Kim, G. D.; Rokade, A. A.; Park, S. S.; Bohara, R. A.; Yu, Y. S. Study of structural and magnetic properties and heat induction of gadolinium-substituted manganese zinc ferrite nanoparticles for *in vitro* magnetic fluid hyperthermia. *J. Colloid Interface Sci.* **2019**, *541*, 192−203.
(20) Almessiere, M. A.; Slimani, Y.; Rehman, S.; Khan, F. A.; Gökçe Polat, E.; Sadaqat, A.; Shirsath, S. E.; Baykal, A. Synthesis of Dy-Y co-substituted manganese-zinc spinel nanoferrites induced anti-bacterial and anti-cancer activities: Comparison between sonochemical and sol-gel auto-combustion methods. *Mater. Sci. Eng., C* **2020**, *116*, No. 111186.
(21) Almessiere, M. A.; Slimani, Y.; Shirsath, S. E.; Wudil, Y. S.; Baykal, A.; Ercan, I. Customized magnetic properties of $(Mn_{0.5}Zn_{0.5})$-$[Eu_xNd_xFe_{2-2x}]O_4$ nanospinel ferrites synthesized via ultrasonic irradiation approach. *Results Phys.* **2020**, *19*, No. 103350.
(22) Almessiere, M. A.; Slimani, Y.; Demir Korkmaz, A.; Güner, S.; Baykal, A.; Shirsath, S. E.; Ercan, I.; Kögerler, P. Sonochemical synthesis of Dy^{3+} substituted $Mn_{0.5}Zn_{0.5}Fe_{2-x}O_4$ nanoparticles: Structural, magnetic and optical characterizations. *Ultrason. Sonochem.* **2020**, *61*, No. 1048362.
(23) Almessiere, M. A.; Trukhanov, A. V.; Khan, F. A.; Slimani, Y.; Tashkandi, N.; Turchenko, V. A.; Zubar, T. I.; Tishkevich, D. I.; Trukhanov, S. V.; Panina, L. V.; Baykal, A. Correlation between microstructure parameters and anti-cancer activity of the $[Mn_{0.5}Zn_{0.5}](Eu_xNd_xFe_{2-2x})O_4$ nanoferrites produced by modified sol-gel and ultrasonic methods. *Ceram. Int.* **2020**, *46*, 7346−7354.
(24) Rehman, S.; Almessiere, M. A.; Khan, F. A.; Demir Korkmaz, A.; Tashkandi, N.; Slimani, Y.; Baykal, A. Synthesis and biological characterization of $Mn_{0.5}Zn_{0.5}Eu_xDy_xFe_{1.8-2x}O_4$ nanoparticles by sonochemical approach. *Mater. Sci. Eng., C* **2020**, *109*, No. 110534.
(25) Weil, L.; Bertaut, E. F.; Bochirol, L. Magnetic properties and structure of the quadratic phase of copper ferrite. *J. Phys. Radium* **1950**, *11*, No. 208.
(26) Cullity, B. D.; Stock, S. R. *Elements of X-ray Diffraction*, 3rd ed.; Pearson: USA, 1956; pp 696.
(27) Klein, L.; Aparicio, M.; Jitianu, A. *Handbook of Sol-Gel Science and Technology*, 2nd ed.; Springer International Publishing: 2018; pp XXXIX, 3789.
(28) Ata-Allah, S. S.; Hashhash, A. Jahn−Teller effect and superparamagnetism in Zn substituted copper-gallate ferrite. *J. Magn. Magn. Mater.* **2006**, *307*, 191−197.
(29) Kumar, H.; Srivastava, R. C.; Singh, J. P.; Negi, P.; Agrawal, H. M.; Das, D.; Chae, K. H. Structural and magnetic study of dysprosium substituted cobalt ferrite nanoparticles. *J. Magn. Magn. Mater.* **2016**, *401*, 6−21.
(30) Naik, P. P.; Tangsali, R. B.; Meena, S. S.; Bhatt, P.; Sonaye, B.; Sugur, S. Gamma radiation roused lattice contraction effects investigated by Mossbauer spectroscopy in nanoparticle Mn−Zn ferrite. *Radiat. Phys. Chem.* **2014**, *102*, 147−152.
(31) Drickamer, H. G.; Frank, C. W. *Electronic Transitions and the High Pressure Chemistry and Physics of Solids*, 1st ed.; Chapman and Hall: London, 1973; pp ix−185.
(32) Zhang, C. F.; Zhong, X. C.; Yu, H. Y.; Liu, Z. W.; Zeng, D. C. Effects of cobalt doping on the microstructure and magnetic properties of Mn−Zn ferrites prepared by the co-precipitation method. *Phys. B* **2009**, *404*, 2327−2331.
(33) Joseyphus, R. J.; Narayanasamy, A.; Shinoda, K.; Jeyadevan, B.; Tohji, K. Synthesis and magnetic properties of the size-controlled Mn−Zn ferrite nanoparticles by oxidation method. *J. Phys. Chem. Solids* **2006**, *67*, 1510−1517.
(34) Baykal, A.; Güner, S.; Demir, A.; Esir, S.; Genç, F. Effect of Zinc substitution on magneto-optical properties of $Mn_{1-x}Zn_xFe_2O_4/SiO_2$ nanocomposites. *Ceram. Int.* **2014**, *40*, 13401−13408.
(35) Baykal, A.; Güner, S.; Demir, A. Synthesis and magneto-optical properties of triethylene glycol stabilized $Mn_{1-x}Zn_xFe_2O_4$ nanoparticles. *J. Alloys Compd.* **2015**, *619*, 5−11.
(36) Cullity, B. D.; Graham, C. D. *Introduction to Magnetic Materials*, 2nd ed.; Wiley-IEEE Press: 2009; pp 568.
(37) Dalal, M. *A Textbook of Inorganic Chemistry*, 1st ed.; Dalal Institute: India, 2017; pp 11−471.
(38) Alves, T. E. P.; Pessoni, H. V. S.; Franco, A., Jr. The effect of Y^{3+} substitution on the structural, optical band-gap, and magnetic properties of cobalt ferrite nanoparticles. *Phys. Chem. Chem. Phys.* **2017**, *19*, 16395−16405.
(39) Stoner, E. C.; Wohlfarth, E. P. A mechanism of magnetic hysteresis in heterogeneous alloys. Philos. *Trans. R. Soc. A* **1948**, *240*, 599−642.
(40) Slimani, Y.; Almessiere, M. A.; Güner, S.; Kurtan, U.; Shirsath, S. E.; Baykal, A.; Ercan, I. Magnetic and microstructural features of Dy^{3+} substituted $NiFe_2O_4$ nanoparticles derived by sol−gel approach. *J. Sol-Gel Sci. Technol.* **2020**, *95*, 202−210.
(41) Khurshid, H.; Kelley, P. L.; Iglesias, O.; Alonso, J.; Phan, M. H.; Sun, C. J.; Saboungi, M. L.; Srikanth, H. Spin-glass-like freezing of inner and outer surface layers in hollow γ-Fe_2O_3 nanoparticles. *Sci. Rep.* **2015**, *5*, No. 15054.

https://doi.org/10.1021/acsomega.1c03416
ACS Omega 2021, 6, 22429−22438